Journal of Materials Chemistry A

ROYAL SOCIETY OF CHEMISTRY

PAPER

View Article Online
View Journal | View Issue

Cite this: J. Mater. Chem. A, 2022, 10, 24793

MXene with controlled surface termination groups for boosting photoelectrochemical water splitting†

Zihao Wu,‡[a] Hui Zong,[b] Baihe Fu[a] and Zhonghai Zhang *[ac]

Received 10th August 2022
Accepted 31st October 2022

DOI: 10.1039/d2ta06313a

rsc.li/materials-a

Interface engineering is a promising strategy to optimize the interfacial photoelectrochemical (PEC) water-splitting system. However, previously, attention was paid to the engineering of the semiconductor/water interface and the other essential interface of the electrode/current collector was seriously undervalued. Herein, MXenes with controllable surface termination groups were synthesized using a molten salt etching method and used as electron transfer layer materials to modulate the interface between the semiconductor and the current collector. With $BiVO_4$ as a model photo-responsive material, the combination of Br-MXene significantly contributed to a 33% increase in the photocurrent density compared with the pristine $BiVO_4$-based photoelectrode. In addition, after attaching cobalt borate (CoBi) as a cocatalyst, the Br-MXene/$BiVO_4$/CoBi photoelectrode achieved a high photocurrent density of 5.47 mA cm^{-2} at 1.23 V *vs.* RHE and photoconversion efficiency of 1.46%. The interface engineering strategy for efficient charge transfer is a promising and universal solution for the rational design of the photoelectrode and will inspire great research enthusiasm in the solar energy conversion fields.

Introduction

After the discovery of hydrogen generation through water splitting using an interfacial photoelectrochemical (PEC) system,[1] a new chapter of artificial photosynthesis research has opened up.[2,3] The PEC system integrates solar light absorption, charge separation, and surface redox conversion in one device. With respect to the construction of the PEC system, the semiconductor-based photoelectrode is the core and vital component, and great efforts have been made to pursue the "ideal" candidates.[4–10] However, most of the semiconductors suffer from inherently low charge carrier mobilities and high non-radiative recombination rates, which severely limit the water-splitting efficiency of PEC. The acceleration of charge transfer and facilitation of the surface redox reaction at the interfaces of the semi-conductor/current collector and the semiconductor/electrolyte are the key aspects to address these concerns. Therefore, interface engineering is regarded as a fully promising solution.[11,12] Previously, most attention was paid to the engineering of the semiconductor/water interface by decorating the hole transport layer (HTL) and surface oxygen/hydrogen evolution catalysts, and a series of effective materials, such as metal/dimetal oxyhydroxides, borates, and phosphates, was well investigated to improve the PEC performance.[13–15] Nevertheless, another essential interface of the electrode/current collector through the introduction of the electron transport layer (ETL) is seriously undervalued. Currently, metal oxides, such as SnO_2, TiO_2, and WO_3 have been directly used as ETL to modulate the heterogeneous interface, however, the high resistance inevitably hinders the efficient transfer of photogenerated electrons.[16]

Considering the rigorous requirements of effective ETL materials, such as excellent conductivity, suitable energy band positions, thin thickness for efficient light transmittance, and large surface areas, two-dimensional nanomaterials are one of the promising candidates to meet these criteria. MXene is a fast-growing family of two-dimensional transition metal carbides, nitrides, and carbonitrides materials, which feature half-metallicity, robust mechanical properties, and high specific surface area.[17–20] Thus, MXenes have attracted enormous interest in many fields.[21–25] However, the conventional MXene synthetic strategy is based on traditional wet chemical methods, which inevitably graft complex surface termination groups of –F, –O, and, –OH, and block the effective control of its electronic properties. Very recently, a molten salt etching method was proposed to prepare MXene with controllable surface termination groups,[26,27] which could modulate the crystal structure and electronic properties of MXene.[28] The rationally designed MXene can be promisingly used as an ETL with the optimized

[a]Shanghai Key Laboratory of Green Chemistry and Chemical Processes, School of Chemistry and Molecular Engineering, East China Normal University, Shanghai 200241, China. E-mail: zhzhang@chem.ecnu.edu.cn

[b]Department of Electronics, Key Laboratory of Polar Materials and Devices (MOE), East China Normal University, Shanghai 200241, China

[c]Institute of Eco-Chongming, East China Normal University, 20 Cuiniao Road, Chongming District, Shanghai 202162, China

† Electronic supplementary information (ESI) available. See DOI: https://doi.org/10.1039/d2ta06313a

‡ Present address: Beijing National Laboratory for Molecular Sciences College of Chemistry and Molecular Engineering, Peking University, Beijing 100871, China.

Fermi level to match the band structure of the target semiconductors for efficient interface charge transfer, and thus improving the PEC performance.

Herein, MXenes with controllable surface termination groups, including chlorine (Cl), bromine (Br), and iodine (I) were fabricated with a molten salt etching method. All of these Cl-MXene, Br-MXene, and I-MXene were used as ETL materials to modulate the interface between the semiconductor and the current collector. In this work, $BiVO_4$ is selected as the model semiconductor due to its advantageous features of favourable band gap, suitable band-edge positions, and high theoretical photocurrent density.[29–32] The interfacial engineering strategy that produced optimized Br-MXene as an ETL significantly contributed to an increase of 33% in photocurrent density compared with the pristine $BiVO_4$-based photoelectrode. In addition, after further attaching an HTL of cobalt borate (CoBi),[33,34] the Br-MXene/$BiVO_4$/CoBi photoelectrode achieved a high photocurrent density of 5.47 mA cm^{-2} at 1.23 V *vs.* RHE and photoconversion efficiency of 1.46%. A series of characteristic experiments and calculation analysis were conducted to elucidate the mechanism of fast electron transfer between MXenes and $BiVO_4$. Therefore, interface engineering can be developed to be a promising and universal strategy for enhancing PEC performance by eliminating the adverse effects of the original conductor–semiconductor mismatch interface.

Results and discussion

The MXenes with Cl, Br and I as the surface termination groups were synthesized with MAX phase Ti_3AlC_2 as a precursor in a newly developed molten salt etching method,[35,36] and the detailed experimental procedures can be found in the Experimental section in ESI.† As shown in Fig. 1a, the anions of molten salts ($CdCl_2$, $CdBr_2$, and CuI) helped remove the aluminum layer of MAX and determined the surface termination groups to form multiple-layer Cl-MXene, Br-MXene, and I-MXene. The representative morphology of the multiple-layer Br-MXene was characterized using scanning electron microscopy (SEM) and atomic-resolution high-angle annular dark-field scanning transmission electron microscopy (HADDF-STEM). Different from the compact layered structure of MAX powder (Fig. S1 in ESI†), the SEM image of molten salt etched Br-MXene sample (Fig. 1b) showed an obvious accordion-like multiple-layer structure and no Cd was left on Br-MXene (Fig. S2 in ESI†). The lamellar microstructure of Br-MXene with the atomic resolution was clearly visible in the HADDF-STEM image (Fig. 1c), and highly-ordered layer-by-layer structures were detected. A closer observation of Br-MXene is presented in Fig. 1d, the typical configuration of two columns of bromine atoms wrapped around three columns of titanium atoms can be clearly seen. Carbon atoms with small atomic masses cannot be detected by this imaging technique. This configuration perfectly fits with the idealized models of the atomic structure of Br-MXene, indicating the successful synthesis of Br-terminated MXene. The elemental distribution of Br-MXene was further demonstrated from the HAADF-STEM image and the corresponding elemental mapping images (Fig. 1e), where Ti, C, and

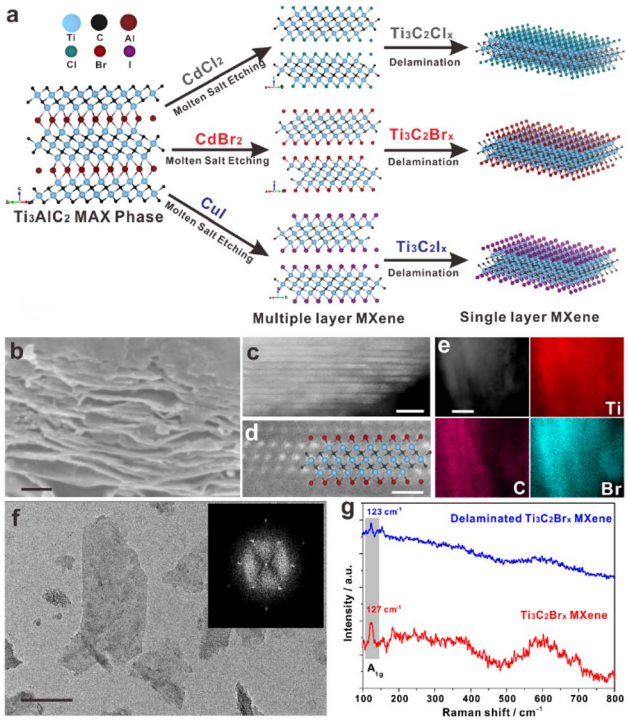

Fig. 1 (a) Schematics of synthesis processes of MXene with halogen termination of Cl, Br, and I, with a molten salt etching method and subsequent ultrasonic delamination procedure; (b) scanning electron microscopy (SEM) image of multiple-layer Br-MXene, the scale bar is 200 nm; (c) atomic-resolution high-angle annular dark-field scanning transmission electron microscopy (HADDF-STEM) image of multiple-layer Br-MXene, the scale bar is 5 nm; (d) enlarged HADDF-STEM image with the well-matched ball-and-stick model of Br-MXene ($Ti_3C_2Br_x$), the scale bar is 1 nm; (e) HAADF-STEM image and the corresponding EDX elemental mapping images of Ti, C, and Br in $Ti_3C_2Br_x$; (f) transmission electron microscope (TEM) image of few-layer Br-MXene, the scale bar is 100 nm, and the inset is Fast Fourier Transform (FFT) of the framed region; (g) Raman spectra of multi-layer and delaminated few-layer Br-MXene.

Br elements are uniformly distributed on Br-MXene. The multiple-layer Br-MXene further underwent the delamination process by sonification and few-layer Br-MXene nanoflakes with typical lateral sizes of several hundred nanometers were obtained (Fig. 1f). The hexagonal symmetric crystallinity of the individual nanoflake was depicted using fast Fourier transform (FFT), and the framed part is presented in the inset of Fig. 1f. MXenes with termination groups of Cl and I were also synthesized and characterized (Fig. S3 and S4 in ESI†).

The surface termination group of Br-MXene was further characterized by Raman spectroscopy. As shown in Fig. 1g, the position of the A_{1g} mode, corresponding to out-of-plane vibration of the surface group,[37] was located at 127 cm^{-1} for multiple layer Br-MXene. The A_{1g} frequency of Br-MXene was much lower than that of the surface-oxygen terminal MXenes (222 cm^{-1}).[26] As the A_{1g} position was primarily determined by the atomic mass of the surface group,[38] the variation in A_{1g} frequency from 222 cm^{-1} to 127 cm^{-1} indicated the successful synthesis of Br-MXene. After the delaminated process, the few-layer Br-MXene

showed a very similar Raman spectrum with a slightly negative shift of A_{1g} peak to 123 cm^{-1}, which suggested that the few-layer Br-MXene largely preserved the functional groups of the corresponding multilayer stacks. Therefore, the thin few-layer MXenes with controlled surface termination groups were prepared. The synthesized MXenes were then redispersed in deionized water to form stable colloid suspensions with a dark greenish color, and an obvious Tyndall scattering effect (Fig. S5 in ESI†) was observed. These colloidal suspensions can be used as stock solutions to prepare efficient photoanodes as ETL materials.

A schematic diagram of the FTO/MXene/$BiVO_4$/CoBi photoanode is illustrated in Fig. 2a. The detailed fabrication procedures can be found in the Experimental section in ESI.† In brief, the colloidal solution containing a few layers MXene was first drop-coated on the FTO substrate. After drying naturally under a nitrogen atmosphere, a transparent MXene thin film was formed on the FTO glass. Secondly, a porous Mo-doped $BiVO_4$ thin film was fabricated on the MXene-coated FTO glass *via* a spin-coating method. Unless otherwise mentioned, all $BiVO_4$ materials used in this work were Mo-doped $BiVO_4$. Third, cobalt borate (CoBi) was subsequently deposited on the top surface of the $BiVO_4$ film to improve the surface reaction kinetics.

The morphology of the $BiVO_4$ thin film was characterized using SEM and TEM images. As shown in Fig. 2b, the $BiVO_4$ exhibited a typical worm-like nanoporous structure, which would contribute to a higher surface area compared to condensed films. The thickness of the $BiVO_4$ film can be determined from the cross-sectional SEM image shown in Fig. 2c, and the thickness of about 390 nm was optimized with the best PEC performances (Fig. S6 in ESI†). The nanoporous structure of $BiVO_4$ was further validated from the TEM image (Fig. 2d), and closer observation from the HRTEM image (Fig. 2e) demonstrated good crystallinity with a clear lattice distance of 0.31 nm, corresponding to the (−121) phase of monoclinic $BiVO_4$. In addition, an amorphous layer can be observed at the outermost edge, which can be assigned to the deposited CoBi. The elemental distribution of $BiVO_4$/CoBi was further characterized from the HAADF-STEM image and the corresponding elemental mapping images are presented in Fig. 2f. Bi, V, O, Mo, Co, B, and merged elemental images indicated the uniform distribution of the elements. The Mo element presented low intensity with an atomic ratio of about 0.5%, which suggested the successful doping of Mo. Furthermore, the conformal existence of Co and B on $BiVO_4$ indicated uniform deposition of CoBi.

The crystal structure of Br-MXene/$BiVO_4$/CoBi was investigated by X-ray diffraction (XRD) and Raman spectroscopy. As shown in Fig. 2g, except for the diffraction peaks from FTO, all other peaks can be assigned to typical monoclinic $BiVO_4$ with a dominated orientation of (−121), which agreed well with the HRTEM result. In addition, no diffraction peaks of MXene and CoBi were found, which can be ascribed to the low crystallinity of the few-layer MXene and amorphous properties of CoBi.[39,40] Furthermore, the Raman spectrum of Br-MXene/$BiVO_4$/CoBi was recorded and is presented in Fig. 2h. The Raman bands at 127 cm^{-1} and 213 cm^{-1} correspond to the external modes (rotation/translation). The bands at 326 cm^{-1} and 368 cm^{-1} can be assigned to the symmetric (A_g) and antisymmetric (B_g) bending modes of the VO_4 tetrahedra, respectively. The most intense (the highest-phonon energy) band centered at 827 cm^{-1} and a weak shoulder at 713 cm^{-1} were attributed to A_g and B_g stretching modes of the V–O bonds in the VO_4 tetrahedra, respectively.[41] All of these Raman bands were characteristic of monoclinic $BiVO_4$. Thus, the existence of MXene as an ETL affected the crystal structure of the $BiVO_4$ film negligibly.

Furthermore, ultraviolet-visible (UV-vis) absorbance spectroscopy was performed to measure the optical properties of Br-MXene/$BiVO_4$/CoBi. As shown in Fig. 2i, the UV-vis spectrum exhibited an absorbance threshold at approximately 500 nm. The combination of MXene and CoBi did not significantly change the optical absorbance of $BiVO_4$. The Tauc plot was then produced to estimate the band gap, which was determined to be 2.63 eV. $BiVO_4$ and MXenes/$BiVO_4$ with different termination groups showed the same band gap values (Fig. S7 in ESI†). To sum up, the FTO/Br-MXene/$BiVO_4$/CoBi photoanode was successfully fabricated, and the MXenes with different termination groups and CoBi did not change the morphology, crystal, and optical absorption properties of $BiVO_4$.

The PEC water oxidation performances of $BiVO_4$-based photoanodes were evaluated under chopped AM 1.5G front illumination in a three-electrode cell with 1 M potassium borate buffer solution (pH = 9.5) as the electrolyte. As presented in Fig. 3a, the $BiVO_4$ photoanode shows a photocurrent density of 3.13 mA cm^{-2} at 1.23 V *vs.* RHE. After the deposition of CoBi on the top surface of $BiVO_4$, the photocurrent density on $BiVO_4$/CoBi was improved to 4.28 mA cm^{-2}. With Br-MXene as ETL to modulate the interface of the semiconductor and current collector, the Br-MXene/$BiVO_4$/CoBi photoanode reached a high

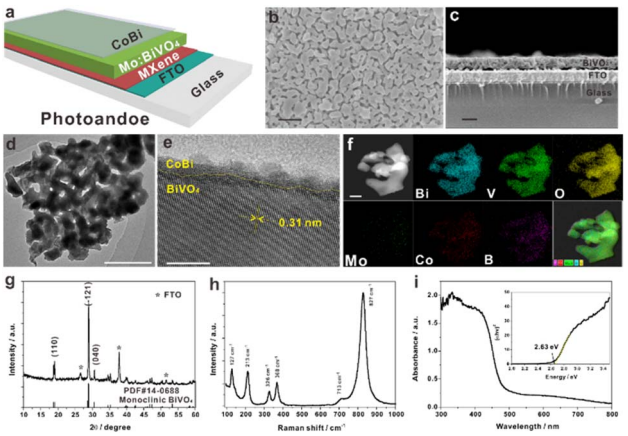

Fig. 2 (a) Schematic of diagram of FTO/Br-MXene/$BiVO_4$/CoBi photoanode; (b) top-view SEM image of Br-MXene/$BiVO_4$/CoBi, the scale bar is 500 nm; (c) cross-sectional SEM image of Br-MXene/$BiVO_4$/CoBi, the scale bar is 500 nm; (d) TEM image of $BiVO_4$/CoBi, the scale bar is 500 nm; (e) HRTEM image of $BiVO_4$/CoBi, the scale bar is 10 nm; (f) HAADF-STEM image and the corresponding EDX elemental mapping images of Bi, V, O, Mo, Co, B, and merged elements; (g) XRD pattern of Br-MXene/$BiVO_4$/CoBi; (h) Raman spectrum of Br-MXene/$BiVO_4$/CoBi; (i) optical absorption spectrum of Br-MXene/$BiVO_4$/CoBi, the inset is the Tauc plot.

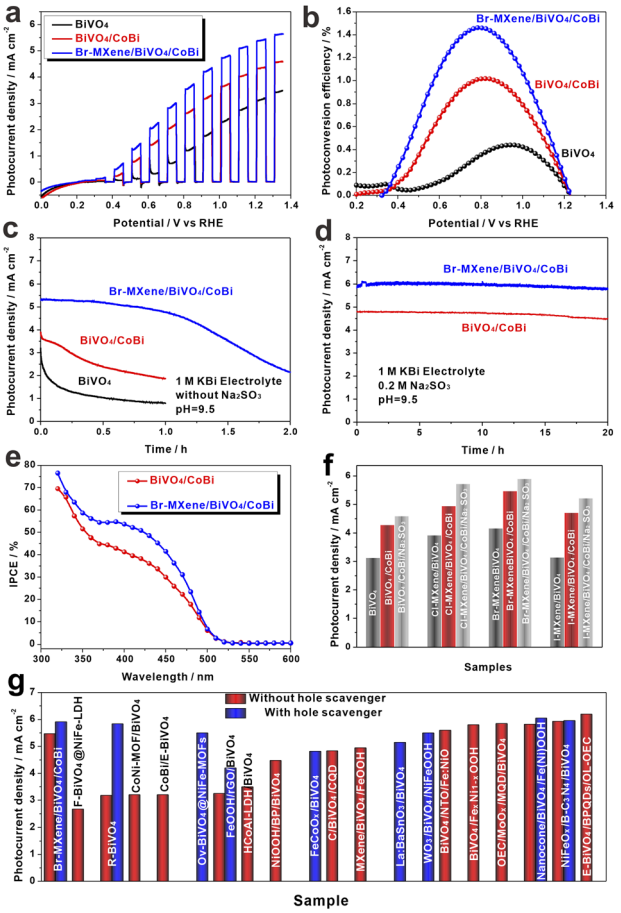

Fig. 3 (a) Chopped LSV curves of pristine $BiVO_4$, $BiVO_4$/CoBi, and Br-MXene/$BiVO_4$/CoBi photoanodes under AM 1.5G illumination; (b) photoconversion efficiency curves of pristine $BiVO_4$, $BiVO_4$/CoBi, and Br-MXene/$BiVO_4$/CoBi; (c) J–t curves for stability measurements on $BiOV_4$, $BiVO_4$/CoBi, and Br-MXene/$BiVO_4$/CoBi in KBi electrolyte without the addition of Na_2SO_3; (d) J–t curves for long-term stability measurements on $BiVO_4$/CoBi and Br-MXene/$BiVO_4$/CoBi in KBi electrolyte with the addition of Na_2SO_3; (e) IPCE curves of $BiVO_4$/CoBi and Br-MXene/$BiVO_4$/CoBi; (f) photocurrent densities at 1.23 V *vs.* RHE on $BiVO_4$, Cl-MXene/$BiVO_4$, Br-MXene-$BiVO_4$, I-MXene-$BiVO_4$ with/without CoBi and with/without hole scavenger of Na_2SO_3 under AM 1.5G illumination; (g) comparison of the photocurrent densities on $BiVO_4$-based photoanodes for PEC water oxidation.

photocurrent density of 5.47 mA cm^{-2} without the hole scavenger. The applied bias-potential photoconversion efficiency (ABPE) of the photoanodes was also evaluated and presented in Fig. 3b. The Br-MXene/$BiVO_4$/CoBi photoanode exhibited an optimal efficiency of 1.46% at 0.79 V *vs.* RHE. The efficiency value on the Br-MXene/$BiVO_4$/CoBi photoanode was much higher than the optimal efficiency of 0.44% at 0.95 V *vs.* RHE on pristine $BiVO_4$. In addition, the stability of the photoanodes was estimated as well. As shown in Fig. 3c, after combining with the ETL of MXene, the stability of $BiVO_4$-based photoanode in the electrolyte in the absence of the sacrificial agent of Na_2SO_3 was improved, which indicated that the fast-electron transfer would suppress the photo-corrosion of pristine $BiVO_4$. While, in the presence of Na_2SO_3, both Br-MXene/$BiVO_4$/CoBi and $BiVO_4$/CoBi photoanodes displayed excellent stability and did not present an obvious decay after 20 h PEC operation (Fig. 3d). The morphological characterization on the photoanodes after the long-term stability test was also performed, and data are presented in Fig. S8 in ESI;† no obvious variation in morphology was detected. Therefore, the increase in photocurrent density, photoconversion efficiency, and stability with Br-MXene as an ETL indicated that interface engineering was an effective strategy for enhancing the PEC performance.

To further reveal the photo-responsive action of $BiVO_4$-based photoanodes at different wavelengths, the incident photon to current efficiency (IPCE) was measured at 1.23 V *vs.* RHE. The IPCE value was estimated and calculated using the following equation:[42]

$$\mathrm{IPCE}\ (\%) = 1240I/\lambda P_{\mathrm{light}} \times 100\% \quad (1)$$

where I is the photocurrent density (mA cm^{-2}), P_{light} is the incident light irradiance (mW cm^{-2}), and λ is the incident light wavelength (nm). As presented in Fig. 3e, both $BiVO_4$/CoBi and Br-MXene/$BiVO_4$/CoBi showed a PEC response threshold at ~500 nm, in accordance with the optical absorption spectrum (Fig. 2i), which suggested that the MXene layer did not play a role in enlarging the light-harvesting range of $BiVO_4$. Br-MXene/$BiVO_4$/CoBi exhibited much higher IPCE values than $BiVO_4$/CoBi. These phenomena indicate that the coupling of ETL can effectively promote charge separation and greatly increases the probability of photoelectron generation.

MXenes with different surface termination groups were employed as ETL to fabricate the $BiVO_4$-based photoanodes, Cl-MXene/$BiVO_4$, Br-MXene/$BiVO_4$, and I-MXene/$BiVO_4$, and the corresponding PEC performances were compared and are presented in Fig. 3f and S9 in ESI.† All MXenes/$BiVO_4$ photoanodes presented higher photocurrent density than pristine $BiVO_4$, and the Br-MXene/$BiVO_4$ presented the highest photocurrent density with/without CoBi. The onset potentials on $BiVO_4$/CoBi, Cl-MXene/$BiVO_4$/CoBi, Br-MXene/$BiVO_4$/CoBi, and I-MXene/$BiVO_4$/CoBi photoanodes were also evaluated, and Br-MXene/$BiVO_4$/CoBi showed the lowest onset potential value (Fig. S10 and Table S1 in ESI†). The different electron mobilities and band energy positions of MXenes with different surface termination groups were responsible for the variation of the PEC performances, and the detailed characterization was performed and is discussed in the later section. In addition, the hole scavenger, Na_2SO_3, was added to the electrolyte for thermodynamically and kinetically expending photo-holes and facilitating charge separation.[43] The corresponding photocurrent density values were recorded (Fig. S10 in ESI†), and Br-MXene/$BiVO_4$/CoBi with Na_2SO_3 contributed to the highest photocurrent density of 5.91 mA cm^{-2} at 1.23 V *vs.* RHE. In addition, the charge separation efficiency on photoanodes with MXene as the electron transfer layer and CoBi as the hole transfer layer was estimated as well (Fig. S11 in ESI†). Finally, the comparison of the PEC water oxidation performances on $BiVO_4$-based photoanodes is summarized and presented in Fig. 3g and Table S2 in ESI.† Br-MXene/$BiVO_4$/CoBi reached a high photocurrent density value, comparable to that of the state-of-the-art $BiVO_4$

photoanodes. Thus, we demonstrated that the interface engineering with MXenes as the ETL was an effective and promising strategy for efficient PEC water oxidation.

A series of calculation analysis and characterization experiments were conducted to reveal the intrinsic electron transfer mechanism between MXene and $BiVO_4$. First, density functional theory (DFT) calculations were performed to reveal the intrinsic conductivity properties and potential electron transfer activity of MXene. As presented in Fig. 4a, the total density of states (TDOS) of Br-MXene and partial density of states (PDOS) of each element were simulated and the one-sided bare Ti resulted in a large number of electrons near the Fermi level. Thus, Br-MXene displayed a typical metallicity due to the incomplete covalent number of Ti. In addition, the introduction of Br terminations made the Ti 4d orbit insufficiently polarized, and thus contributed to the decrease of the Fermi level.[44] Furthermore, the three-dimensional differential charge density diagram of Br-MXene/$BiVO_4$ was simulated and calculations were performed. The distance between Ti and Br atoms is 2.44 Å, larger than the distance between the traditional O-terminal group and the F-terminal group and Ti in MXene. The large distance could be related to the fact that the electronegativity of Br was smaller than that of O and F.[45–48] As presented in Fig. 4b, yellow areas represent the charge accumulation region, and light blue areas indicate a charge depletion region. The O atoms in $BiVO_4$ exhibited an obvious scenario of gathering electrons from Bi and V atoms,[49] transferring these electrons from O atoms in $BiVO_4$ to the Br atoms in MXene. The DFT calculation results indicated that photo-generated electrons in $BiVO_4$ can be expected to efficiently transfer to Br-MXene, and thus facilitate the charge separation.

To further understand the intrinsic mechanism of the electron transfer between MXene and $BiVO_4$, core-level X-ray photoelectron spectra (XPS) of Bi 4f, V 2p, and O 1s of $BiVO_4$ and Br-MXene/$BiVO_4$ were measured and are presented in Fig. 4c–e, respectively. The Bi 4f XPS of pristine $BiVO_4$ showed two typical peaks with binding energies at 164.3 eV and 159.0 eV, assigned to Bi $4f_{5/2}$ and Bi $4f_{7/2}$ respectively,[50] whose values have been positively shifted to 164.8 eV and 159.5 eV for Bi 4f of Br-MXene/$BiVO_4$. The V 2p XPS of $BiVO_4$ depicted binding energy peaks at 524.0 eV and 516.6 eV, which can be ascribed to V $2p_{3/2}$ and V $2p_{1/2}$, respectively.[51] After the combination of Br-MXene with $BiVO_4$, the binding energies of O 1s shifted to higher values of 524.4 eV and 517.1 eV. Furthermore, the core-level XPS of O 1s was measured, and the O 1s XPS of $BiVO_4$ presented a strong peak with the binding energy of 529.7 eV, which can be ascribed to the O atom in the monoclinic bond of $[Bi_2O_2]^{2+}$. In addition, another peak with low intensity located at 530.7 eV can be associated with the O_2^- ion of the oxygen defects on the $BiVO_4$ surface.[52] For Br-MXene/$BiVO_4$, the binding energy of oxygen in the lattice was increased to 530.1 eV. Another peak at 532.5 eV can be considered to be loosely bound oxygen on the surface of $BiVO_4$. No oxygen vacancy defects can be detected in Br-MXene/$BiVO_4$. Therefore, the XPS data presented a positive shift of binding energies of Bi 4f, V 2p, and O 1s on MXene/$BiVO_4$, compared with $BiVO_4$, which implied the decrease in electron cloud density on $BiVO_4$ and revealed charge transfer from $BiVO_4$ to Br-MXene.

Besides DFT calculations and XPS measurements to reveal electron transfer at the micro-level between Br-MXene and $BiVO_4$, the macro-performance of electron transfer should be further characterized through optical and electrochemical measurements. First, the fluorescence emission spectrum of photoelectrode was a potential solution to monitor the charge separation tendency. The fluorescence was generated from the radiative recombination of photogenerated carriers, thus lower fluorescence intensity of the photoelectrode implied better charge separation efficiency. As presented in Fig. 4f, Br-MXene/$BiVO_4$ showed much lower fluorescence intensity than pristine $BiVO_4$, which revealed that the combination of MXene layers can help suppress the recombination of photogenerated carriers due to the potential charge carrier transfer between MXene and $BiVO_4$. In addition, electrochemical impedance spectra (EIS) were recorded to evaluate the charge transfer process. The Nyquist plots of $BiVO_4$ with/without MXene are shown in Fig. 4g. The circular radius of the Nyquist curves corresponds to the charge transfer resistance. The MXenes coupled $BiVO_4$ presented smaller circular radii than pristine $BiVO_4$, and Br-MXene/$BiVO_4$ showed the lowest charge transfer resistance. Furthermore, the electron lifetime (τ) was determined from the Bode-phase plots (inset in Fig. 4g). The Bode-phase plots of Br-MXene/$BiOV_4$ presented a lower characteristic

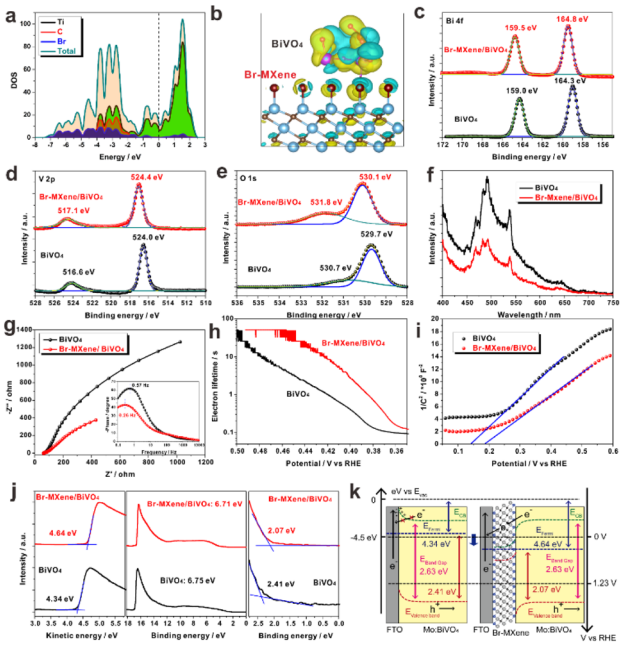

Fig. 4 (a) DOS of Br-MXene; (b) DFT calculation of the charge density difference on the interface of Br-MXene/$BiVO_4$; core-level XPS spectra of (c) Bi 4f, (d) V 2p, and (e) O 1s of $BiVO_4$ and Br-MXene/$BiVO_4$; (f) fluorescence spectrum of $BiVO_4$ and Br-MXene/$BiVO_4$; (g) Nyquist plots of $BiVO_4$ and Br-MXene/$BiVO_4$, the inset is bode plots of $BiVO_4$ and Br-MXene/$BiVO_4$; (h) electron lifetime curves of $BiVO_4$ and Br-MXene/$BiVO_4$; (i) Mott–Schottky plots of $BiVO_4$ and Br-MXene/$BiVO_4$; (j) UPS and valence spectra of $BiVO_4$ and Br-MXene/$BiVO_4$; (k) proposed interface charge transport mechanism of $BiVO_4$ and the Br-MXene/$BiVO_4$ heterojunction with energy band structure.

frequency (0.26 Hz) than pristine $BiVO_4$ (0.57 Hz), which implied a longer electron lifetime on Br-MXene/$BiOV_4$.[53] The electron lifetime was measured by an open circuit photovoltage (V_{oc}) decay method. The V_{oc} curves were measured by turning off the illumination under the steady-state conditions to give a decaying curve (Fig. S12 in ESI†), and the electron lifetime could be calculated using the following equation:[5]

$$\tau = (k_B T/e)\left(\frac{dV_{oc}}{dt}\right)^{-1} \quad (2)$$

where τ is the lifetime of photoelectrons, V_{oc} is the open circuit photovoltage value at time t, k_B is the Boltzmann's constant, T is the temperature, and e is the charge of a single electron. As shown in Fig. 4h, the calculated τ values as a function of V_{oc} clearly indicated that Br-MXene/$BiVO_4$ presented a significantly longer lifetime of the photoelectrons than that of the $BiVO_4$.

In addition, the electrochemical capacitance was measured and the corresponding Mott–Schottky (M–S) plots of $BiVO_4$ and MXene/$BiVO_4$ are presented in Fig. 4i and S13 in ESI.† $BiVO_4$ and MXene/$BiVO_4$ maintained n-type semiconductor features with positive slopes. The carrier density and flat band potentials of the different samples can be calculated using the following equation and the results are listed in Table S3 in ESI:† [54]

$$N_D = -\left(\frac{2}{e\varepsilon_0\varepsilon}\right)\left[\frac{d(1/C^2)}{d(U_s)}\right]^{-1} \quad (3)$$

Compared with $BiVO_4$, all MXene/$BiVO_4$ samples showed higher carrier densities, and Br-MXene/$BiVO_4$ exhibited the highest carrier density. The flat band potential of Br-MXene/$BiVO_4$ depicted a positive shift from 0.143 V of pristine $BiVO_4$ to 0.187 V, which can be attributed to the decrease in the Fermi level due to the oriented electron transfer through the ETL of MXene. All of the above results indicate the advantages of MXenes as ETL to accelerate electron transfer and suppress photocarrier recombination.

In order to gain deeper insight into the intrinsic energy structures of $BiVO_4$ and MXene/$BiVO_4$, ultraviolet photoelectron spectroscopy (UPS) measurements were performed to undergo a more detailed analysis of the band structure of $BiVO_4$-based photoanode. The work functions (Φ, relative energy between the Fermi level and the vacuum level) and the relative electron binding energies between the valence band maximum and the Fermi level ($E_{VB} - E_F$) of $BiVO_4$ and Br-MXene/$BiVO_4$ were measured and are presented in Fig. 4j. The values on Cl-MXene/$BiVO_4$ and I-MXene/$BiVO_4$ samples are shown in Fig. S14 in ESI.† The work functions of Br-MXene/$BiVO_4$ increased to 4.64 eV from 4.34 eV of $BiVO_4$, which indicated that the Fermi levels dropped down due to the electrons transferring away from $BiVO_4$ through the ETL of MXene. In addition, the order of the magnitude of the work functions of MXenes/$BiVO_4$ samples was consistent with the PEC performance, further revealing that the efficient electron transfer through ETL was responsible for the increased PEC performance. Through the UPS and M–S results, the Br-MXene/$BiVO_4$/CoBi photoanode presented better PEC performance than Cl-MXene/$BiVO_4$/CoBi, and I-MXene/$BiVO_4$/CoBi photoanodes can be ascribed to the proper work function position and suitable electron affinity of Br. Based on the UPS data and Tauc plot (inset in Fig. 2i), the energy band structures of $BiVO_4$ and Br-MXene/$BiVO_4$ are illustrated and presented in Fig. 4k. The Schottky junction between the $BiVO_4$ semiconductor and FTO conductive substrate spontaneously led to the Fermi-level pinning and an unavoidable Schottky barrier, which suppressed photogenerated electron transport through the interface. After combination with Br-MXene as the ETL, the metal–semiconductor interaction between FTO and $BiVO_4$ was decoupled and the electron transport at the interface was unimpeded, which significantly improved the carrier separation efficiency and contributed to the efficient PEC performance.

Experimental

Synthesis of Cl-MXene and Br-MXene

Ti_3AlC_2 MAX phase was mixed with anhydrous $CdCl_2$/$CdBr_2$ salts with a 1 : 8 molar ratio using a mortar and pestle. The resultant mixture was then placed in an alumina crucible followed by loading it into a tube furnace. Before heating, argon gas was purged for 30 min to remove the remaining air in the tube furnace. Molten salt etching was then performed at 650 °C for 6 h for Cl-terminated MXene and 610 °C for 6 h for Br-terminated MXene. After cooling, the resultant was dissolved in concentrated aqueous HCl (for Cl-terminated MXene) or concentrated aqueous HBr (for Br-terminated MXene) and stirred for 24 h to remove excess $CdCl_2$/$CdBr_2$ and Cd metal. MXene powder was recovered after washing with deionized water until neutral pH and vacuum drying at 45 °C for 12 h.

Synthesis of I-MXene

The Ti_3AlC_2 MAX phase was mixed with anhydrous CuI salts in a 1 : 6 molar ratio using a mortar and pestle. Molten salt etching was performed at 700 °C for 7 h in a tube furnace. The resultant mixture was then dissolved in an excessive volume of concentrated ammonia and stirred for 24 h to remove excess CuI and Cu metal. I-MXene was recovered after washing with deionized water until neutral pH and vacuum drying at 45 °C for 12 h.

Delamination of MXenes

In a typical delamination process, 100 mg molten salt etching MXenes were placed into a 1.5 mL DMSO solution. Then, the mixture was sealed and stirred at room temperature for 72 h. DMSO-intercalated MXene powder was then immersed in 10 mL of anhydrous NMF to undergo the sonification process for 5 h. The supernatant was centrifuged at 3500 rpm for 1 h to remove the multiple-layer MXene. Then, the supernatant was centrifuged at 9000 rpm for 1 h to remove small impurities. Finally, the sediment was dispersed in deionized water to form stable colloidal solutions of MXene nanoflakes.

Fabrication of photoanodes

The Mo-doped $BiVO_4$ films were fabricated following a simple spin-coating method and all synthesis procedures were carried out in air (Fig. S15 in ESI†). In a typical synthesis process, the

$BiVO_4$ precursor solution was prepared using the following procedures: (1) 0.600 mmol (0.291 g) $Bi(NO_3)_3 \cdot 5H_2O$ and 0.012 mmol (0.0039 g) $MoO_2(acac)_2$ were dissolved in 500 μL of ethylene glycol and stirred for 15 min; (2) 1.5 mL of glacial acetic acid and 0.30 mL of deionized water were added sequentially to the solution and sonicated for 5 min to obtain a clear and colourless solution; (3) 1.200 mmol (0.318 g) $VO(acac)_2$ was added and then sonicated for another 20 min to dissolve it sufficiently; (4) 350 mg of the triblock copolymer pluronic F-108 was added as a structure directing agent for the nanoporous $BiVO_4$ films; (5) $BiVO_4$ thin film photoanodes were deposited on cleaned FTO substrates at 600 rpm for 30 s followed by 1200 rpm for 10 s and baking at 150 °C for 5 min to obtain precursor gel films; (6) the films were annealed in a muffle furnace at 475 °C for 15 min at a heating rate of 10 °C min^{-1}; (7) 1 M KOH was used to remove the excess V_2O_5 from the film surface.

CoBi cocatalyst

CoBi deposition was performed in a three-electrode PEC cell containing 1 M potassium borate electrolyte (pH = 9.5) with 0.5 mM $Co(NO_3)_2 \cdot 6H_2O$. A platinum foil electrode was used as the counter electrode and an Ag/AgCl electrode was used as the reference electrode. With the assistance of AM 1.5G illumination (front illumination), Cobi cocatalyst was deposited at 1.2 V *vs.* RHE for 5 s on the fresh $BiVO_4$ films or MXene-$BiVO_4$ films, hence the $BiVO_4$-CoBi and MXene-$BiVO_4$/CoBi photoanodes were fabricated.

Material characterization

The morphologies of the samples were characterized using SEM (S4800, Hitachi), TEM (JEOLJEM 2100), and HAADF-STEM (JEM-ARM300F). The crystalline structure and chemical structure of the samples were analyzed using X-ray diffraction (XRD) (a Bruker D8 Discover diffractometer using Cu Kα radiation (1.540598 Å)) and a DXR Raman Microscope (ThermoFisher Scientific). XPS data were collected using an Axis Ultra instrument (Kratos Analytical) under an ultrahigh vacuum ($<10^{-8}$ torr) and using a monochromatic Al Kα X-ray source with binding energies referenced to the C 1s binding energy of 284.8 eV. The UPS measurements were conducted using an ultrahigh vacuum surface analysis system equipped with a SCIENTA R3000 spectrometer with a base pressure of 10^{-10} mbar. The diffuse reflectance UV-vis absorption spectra were recorded on a spectrophotometer (Shimadzu, UV 3600) using $BaSO_4$ powder as a reference. Photoluminescence (PL) emission spectra were measured using a photoluminescence spectrometer (FLS980, Edinburgh Instruments Ltd). The electrochemical characterizations of electrochemical impedance spectra (EIS) and capacity were measured using a PGSTAT 302N Autolab Potentiostat/Galvanostat (Metrohm) equipped with an excitation signal of 10 mV amplitude, and the Mott–Schottky measurements were performed at a fixed frequency of 1 kHz.

PEC performance

PEC performance of the obtained photoanodes was measured using a standard three-electrode system on an electrochemical workstation (CHI660d, CH Instruments, Inc.). The counter and reference electrodes were platinum foil and Ag/AgCl (saturated KCl) electrodes, respectively. 1 M potassium borate (pH = 9.5) without or with 0.1 M Na_2SO_3 as the hole scavenger was used as the electrolyte for all PEC measurements. The light source was a Xe 150 W lamp and it was equipped with an AM 1.5 G filter and the light intensity was carefully calibrated to 100 mW cm^{-2}. The recorded potentials were converted against the reversible hydrogen electrode (RHE) using the Nernst equation:

$$E_{vs.\ \mathrm{RHE}} = E_{vs.\ \mathrm{Ag/AgCl}} + E^{\theta}_{\mathrm{Ag/AgCl}} + 0.059 \times \mathrm{pH}$$

The incident photoelectron conversion efficiency (IPCE) was measured at 1.23 V *versus* RHE in the same three-electrode system used above with 1 M potassium borate (pH = 9.5) without any hole scavenger as the electrolyte.

Conclusions

In summary, the MXenes with controllable surface termination groups of chlorine, bromine, and iodine were synthesized and used as the ETL to facilitate effective charge separation. After the combination of CoBi as the cocatalyst, the Br-MXene/$BiVO_4$/CoBi photoanode reached a high photocurrent density of 5.47 mA cm^{-2} at 1.23 V *vs.* RHE. This value was comparable to the state-of-the-art PEC performance of the $BiVO_4$-based photoanodes. A series of characterization measurements and DFT calculations helped reveal the intrinsic electron transfer mechanism between MXene and $BiVO_4$, and the superior photogenerated carrier transfer kinetics and electron–hole pair separation efficiency through MXene as ETL was responsible for the efficient PEC performance. We believe that the novel interface engineering strategy between the semiconductor and the current collector will boost further investigation enthusiasm on PEC water splitting through the rational design of photoelectrodes.

Author contributions

Z. W. and Z. Z. designed the experiments. Z. W. and B. F. carried out experiments on photoanode fabrication and PEC measurements. H. Z. performed the DFT calculation. All authors wrote the manuscript.

Conflicts of interest

The authors declare no competing financial interest.

Acknowledgements

This research was supported by the National Natural Science Foundation of China (No. 22174045, 21822403, 21775045). We want to thank the support from Ruijuan Qi for morphological characterizations, and Prof. Qinye Bao and Dr Jianming Yang for the UPS measurements and valuable discussions.

References

1 A. Fujishima and K. Honda, *Nature*, 1972, **238**, 37–38.
2 K. Sivula and R. van de Krol, *Nat. Rev. Mater.*, 2016, **1**, 15010.
3 J. Kibsgaard and I. Chorkendorff, *Nat. Energy.*, 2019, **4**, 430–433.
4 Z. Zhang, L. Zhang, M. N. Hedhili, H. Zhang and P. Wang, *Nano Lett.*, 2013, **13**, 14–20.
5 Z. Zhang, R. Dua, L. Zhang, H. Zhu, H. Zhang and P. Wang, *ACS Nano*, 2013, **7**, 1709–1717.
6 Z. Zhang and P. Wang, *Energy Environ. Sci.*, 2012, **5**, 6506–6512.
7 J. M. Yu, J. Lee, Y. S. Kim, J. Song, J. Oh, S. M. Lee, M. Jeong, Y. Kim, J. H. Kwak, S. Cho, C. Yang and J. W. Jang, *Nat. Commun.*, 2020, **11**, 5509.
8 J. Fu, Z. Fan, M. Nakabayashi, H. Ju, N. Pastukhova, Y. Xiao, C. Feng, N. Shibata, K. Domen and Y. Li, *Nat. Commun.*, 2022, **13**, 729.
9 I. Roger, M. A. Shipman and M. D. Symes, *Nat. Rev. Chem.*, 2017, **1**, 0003.
10 S. Wang, G. Liu and L. Wang, *Chem. Rev.*, 2019, **119**, 5192–5247.
11 Y. Kuang, T. Yamada and K. Domen, *Joule*, 2017, **1**, 290–305.
12 M. A. Gaikwad, U. P. Suryawanshi, U. V. Ghorpade, J. S. Jang, M. P. Suryawanshi and J. H. Kim, *Small*, 2022, **18**, 2105084.
13 A. S. M. Ismail, I. Garcia-Torregrosa, J. C. Vollenbroek, L. Folkertsma, J. G. Bomer, T. Haarman, M. Ghiasi, M. Schellhorn, M. Nachtegaal, M. Odijk, A. van den Berg, B. M. Weckhuysen and F. M. F. de Groot, *ACS Catal.*, 2021, **11**, 12324–12335.
14 H. Xu, W. Fan, Y. Zhao, B. Chen, Y. Gao, X. Chen, D. Xu and W. Shi, *Chem. Eng. J.*, 2021, **411**, 128480.
15 Y. Fan, X. Ning, Q. Zhang, H. Zhao, J. Liu, P. Du and X. Lu, *ChemSusChem*, 2021, **14**, 1414–1422.
16 A. Venugopal, R. Kas, K. Hau and W. A. Smith, *J. Am. Chem. Soc.*, 2021, **143**, 18581–18591.
17 M. Naguib, M. Kurtoglu, V. Presser, J. Lu, J. Niu, M. Heon, L. Hultman, Y. Gogotsi and M. W. Barsoum, *Adv. Mater.*, 2011, **23**, 4248–4253.
18 M. Naguib, V. N. Mochalin, M. W. Barsoum and Y. Gogotsi, *Adv. Mater.*, 2014, **26**, 992–1005.
19 M. Alhabeb, K. Maleski, B. Anasori, P. Lelyukh, L. Clark, S. Sin and Y. Gogotsi, *Chem. Mater.*, 2017, **29**, 7633–7644.
20 S. Wan, X. Li, Y. Chen, N. Liu, S. Dou, L. Jiang and Q. Cheng, *Science*, 2021, **374**, 96–99.
21 Y. Pei, X. Zhang, Z. Hui, J. Zhou, X. Huang, G. Sun and W. Huang, *ACS Nano*, 2021, **15**, 3996–4017.
22 R. Li, L. Zhang, L. Shi and P. Wang, *ACS Nano*, 2017, **11**, 3752–3759.
23 K. Li, M. Liang, H. Wang, X. Wang, Y. Huang, J. Coelho, S. Pinilla, Y. Zhang, F. Qi, V. Nicolosi and Y. Xu, *Adv. Funct. Mater.*, 2020, **30**, 2000842.
24 Y. Z. Zhang, J. K. El-Demellawi, Q. Jiang, G. Ge, H. Liang, K. Lee, X. Dong and H. N. Alshareef, *Chem. Soc. Rev.*, 2020, **49**, 7229–7251.
25 X. Li, Z. Huang, C. E. Shuck, G. Liang, Y. Gogotsi and C. Zhi, *Nat. Rev. Chem.*, 2022, **6**, 389–404.
26 V. Kamysbayev, A. S. Filatov, H. Hu, X. Rui, F. Lagunas, D. Wang, R. F. Klie and D. V. Talapin, *Science*, 2020, **369**, 979–983.
27 Y. Li, H. Shao, Z. Lin, J. Lu, L. Liu, B. Duployer, P. O. Å. Persson, P. Eklund, L. Hulman, M. Li, K. Chen, X. H. Zha, S. Du, P. Rozier, Z. Chai, E. Raymundo-Piñero, P. L. Taberna, P. Simon and Q. Huang, *Nat. Mater.*, 2020, **19**, 894–899.
28 J. L. Hart, K. Hantanasirisakul, A. C. Lang, B. Anasori, D. Pinto, Y. Pivak, J. T. van Omme, S. J. May, Y. Gogotsi and M. L. Taheri, *Nat. Commun.*, 2019, **10**, 522.
29 T. W. Kim and K. S. Choi, *Science*, 2014, **343**, 990–994.
30 B. Zhang, X. Huang, Y. Zhang, G. Lu, L. Chou and Y. Bi, *Angew. Chem., Int. Ed.*, 2020, **59**, 18990–18995.
31 B. Zhang, S. Yu, Y. Dai, X. Huang, L. Chou, G. Lu, G. Dong and Y. Bi, *Nat. Commun.*, 2021, **12**, 6969.
32 B. Jin, Y. Cho, C. Park, J. Jeong, S. Kim, J. Jin, W. Kim, L. Wang, S. Lu, S. Zhang, S. H. Oh, K. Zhang and J. H. Park, *Energy Environ. Sci.*, 2022, **15**, 672–679.
33 F. Niu, Q. Zhou, Y. Han, R. Liu, Z. Zhao, Z. Zhang and K. Hu, Rapid Hole Extraction Based on Cascade Band Alignment Boosts Photoelectrochemical Water Oxidation Efficiency, *ACS Catal.*, 2022, **12**, 10028–10038.
34 S. Wang, P. Chen, J. H. Yun, Y. Hu and L. Wang, An Electrochemically Treated $BiVO_4$ Photoanode for Efficient Photoelectrochemical Water Splitting, *Angew. Chem., Int. Ed.*, 2017, **56**, 8500–8504.
35 M. Li, J. Lu, K. Luo, Y. Li, K. Chang, K. Chen, J. Zhou, J. Rosen, L. Hultman, P. Eklund, P. O. Å. Persson, S. Du, Z. Chai, Z. Huang and Q. Huang, *J. Am. Chem. Soc.*, 2019, **141**, 4730–4737.
36 L. Liu, M. Orbay, S. Luo, S. Duluard, H. Shao, J. Harmel, P. Rozier, P. L. Taberna and P. Simon, *ACS Nano*, 2022, **16**, 111–118.
37 A. Sarycheva and Y. Gogotsi, *Chem. Mater.*, 2020, **32**, 3480–3488.
38 T. Hu, M. Hu, B. Gao, W. Li and X. Wang, *J. Phys. Chem. C*, 2018, **122**, 18501–18509.
39 A. Jawaid, A. Hassan, G. Neher, D. Nepal, R. Pachter, W. J. Kennedy, S. Ramakrishnan and R. A. Vaia, *ACS Nano*, 2021, **15**, 2771–2777.
40 D. Xue, M. Kan, X. Qian and Y. Zhao, *ACS Sustainable Chem. Eng.*, 2018, **6**, 16228–16234.
41 Y. K. Kshetri, B. Chaudhary, T. Kamiyama, T. H. Kim, F. Rosei and S. W. Lee, *Mater. Lett.*, 2021, **291**, 129519.
42 Y. Zhao, W. Wu, B. Fu, L. Gan and Z. Zhang, *Chin. J. Chem.*, 2020, **38**, 275–281.
43 J. B. Pan, B. H. Wang, J. B. Wang, H. Z. Ding, W. Zhou, X. Liu, J. R. Zhang, S. Shen, J. K. Guo, L. Chen, C. T. Au, L. L. Jiang and S. F. Yin, *Angew. Chem., Int. Ed.*, 2021, **60**, 1433–1440.
44 G. Li, N. Li, S. Peng, B. He, H. Wang, Y. Du, W. Zhang, K. Han and F. Dang, *Adv. Energy Mater.*, 2020, **11**, 2002721.
45 K. A. Papadopoulou, D. Parfitt, A. Chroneos and S. R. G. Christopoulos, *J. Appl. Phys.*, 2021, **130**, 095101.

46 Y. Yang, M. Yao, X. Wang and H. Huang, *J. Phys. Chem. C*, 2019, **123**, 17466–17471.
47 Z. Wang, X. Chen, F. Shen, X. Hang and C. Niu, *Adv. Theory Simul.*, 2018, **1**, 1800059.
48 A. Lee, D. Krishnamurthy and V. Viswanathan, *ChemSusChem*, 2018, **11**, 1911–1918.
49 Y. Fang, Y. Cao, B. Tan and Q. Chen, *ACS Appl. Mater. Interfaces*, 2021, **13**, 42624–42634.
50 Z. Tian, P. Zhang, P. Qin, D. Sun, S. Zhang, X. Guo, W. Zhao, D. Zhao and F. Huang, *Adv. Energy Mater.*, 2019, **9**, 1901287.
51 C. Liu, J. Zhou, J. Su and L. Guo, *Appl. Catal., B*, 2019, **241**, 506–513.
52 J. Xu, Z. Bian, X. Xin, A. Chen and H. Wang, *Chem. Eng. J.*, 2018, **337**, 684–696.
53 H. Anwer, H. Lee, H. R. Kim, H. K. Kim and J. W. Park, *Appl. Catal., B*, 2020, **265**, 118564.
54 Z. Li, X. Zhou, J. Yang, B. Fu and Z. Zhang, *ACS Appl. Mater. Interfaces*, 2019, **11**, 21417–21423.